Imaging connected porosity of crystalline rock by contrast agent-aided X-ray microtomography and scanning electron microscopy

J. Kuva[a,b], J. Sammaljärvi[b*], J. Parkkonen[a], M. Siitari-Kauppi[b], M. Lehtonen[c], T. Turpeinen[d], J. Timonen[a], M. Voutilainen[b]

*: Corresponding author

a: University of Jyväskylä, Department of Physics, P.O. Box 35, 40014 University of Jyväskylä, Finland, , jukka.kuva@iki.fi, joni.parkkonen@jyu.fi, jussi.t.timonen@jyu.fi

b: University of Helsinki, Department of Chemistry, P.O. Box 55, 00014 University of Helsinki, Finland, +348504486642, juuso.sammaljarvi@helsinki.fi, marja.siitari-kauppi@helsinki.fi, ma.voutilainen@helsinki.fi

c: Geological Survey of Finland, Betonimiehenkuja 4, 02151 Espoo, Finland, marja.lehtonen@gtk.fi

d: VTT Technical Research Centre of Finland Ltd, P.O. Box 1603, 40101 Jyväskylä, Finland, tuomas.turpeinen@vtt.fi

Keywords: X-ray microtomography, Scanning electron microscopy, Energy dispersive X-ray spectrometry, Connected porosity, Crystalline rock

Abstract

We set out to study connected porosity of crystalline rock using X-ray microtomography and scanning electron microscopy with energy dispersive X-ray spectroscopy (SEM-EDS) with caesium chloride as a contrast agent. Caesium is an important radionuclide regarding the final deposition of nuclear waste and also forms dense phases that can be readily distinguished by X-ray microtomography and SEM-EDS. Six samples from two sites, Olkiluoto (Finland) and Grimsel (Switzerland), where transport properties of crystalline rock are being studied in-situ, were

investigated using X-ray microtomography and SEM-EDS. The samples were imaged with X-ray microtomography, immersed in a saturated caesium chloride (CsCl) solution for 141, 249 and 365 days and imaged again with X-ray microtomography. CsCl inside the samples was successfully detected with X-ray microtomography and it had completely penetrated all six samples. SEM-EDS elemental mapping was used to study the location of caesium in the samples in detail with quantitative mineral information. Precipitated CsCl was found in the connected pore space in Olkiluoto veined gneiss and in lesser amounts in Grimsel granodiorite. Only a very small amount of precipitated CsCl was observed in the Grimsel granodiorite samples. In Olkiluoto veined gneiss caesium was found in pinitised areas of cordierite grains. In the pinitised areas caesium was found in notable excess compared to chloride, possibly due to the combination of small pore size and negatively charged surfaces. In addition, elevated concentrations of caesium were found in kaolinite and sphalerite phases. The findings concerning the location of CsCl were congruent with X-ray microtomography.

Lay abstract

Crystalline rocks have small amount of empty space, porosity, in them. This porosity has large influence on the properties of the rock and therefore its applications. Different techniques exists to visualize this pore space. In this work we have used X-ray tomography and Scanning Electron Microscopy with Energy Dispersive X-ray Spectroscopy (SEM-EDS). As the pores in crystalline rock usually have diameters of few micrometres or less, it is difficult to see them without something to enhance the contrast and highlight the pore space. Therefore we tested a method to highlight the pore space with a contrast agent introduced via saturated water solution, which forms dense phases that are clearly visible in both X-ray tomography and SEM-EDS. We used CsCl as a contrast agent in two different types of crystalline rock samples. Different immersion times were used to test the speed in which the contrast agent intrudes into the pores of the rock. The samples were dried after

the immersion. Thereafter methyl methacrylate was intruded into the sample and polymerised therein to fix the CsCl in place. The results showed that CsCl phases highlighted the connected pore space of the rock in both X-ray tomography and SEM-EDS. Open fissures showed improved contrast and especially noteworthy contrast improvement was noted in cordierite that had undergone alteration to pinite, a mixture of clay minerals. In pinite it was also noted that caesium was found often in considerably higher abundance than its counter ion chloride. This was probably because due to chloride's negative charge, it was excluded from the smallest pores with negatively charged surfaces.

1. INTRODUCTION

The microstructure of rock has been studied for decades with various methods and motivations (McWilliams 1966; Hoagland, et al. 1973; Vernon 2004; Zabler, et al. 2008; Kuva, et al. 2012). Computed X-ray microtomography (Radon 1917; Cormack 1963; Hounsfield 1973; Kak and Slanley 2001; Stock 2009; Maire and Withers 2014), a method that was first used for medical purposes (Hounsfield 1973), has been widely used to study geological samples (Zabler, et al. 2008; Kuva, et al. 2012; Cnudde & Boone 2013; Wildenschild and Sheppard 2013; Jacques, et al. 2014; Thiemeyer, et al. 2015). It is a powerful method, which can non-invasively obtain three dimensional density maps of rock samples. The method has relatively recently become so accurate, that it has been used to determine material parameters such as porosity (Farber, et al. 2003), grain size distribution (Thovert, et al. 2001), tortuosity (Gommes, et al. 2009) and permeability (Gouze and Luquot 2011). These parameters characterize the structure and transport properties of rock, but unfortunately the resolution of the method is not good enough for a detailed analysis of sub-micrometre features of centimetre scale low porous geological samples. X-ray microtomography can, however, be improved by using a marker fluid with a high X-ray attenuation coefficient (Ketcham and Iturrino 2005; Singh, et al. 2011; Bultreys, et al. 2015) or combining it with

complementary methods, such as the ^{14}C-polymethylmethacrylate (C-14-PMMA) autoradiography technique (Hellmuth, et al. 1993; Voutilainen, et al. 2012). Due to recent progress in laboratory equipment and with the use of synchrotron radiation (Fusseis, et al. 2014) computed microtomography has become fast enough to obtain “four dimensional” images, that are able to show temporal changes in three dimensional images (Mokso, et al. 2011; Lowe, et al. 2013; Eastwood, et al. 2014; Bultreys, et al. 2015).

SEM (Nixon 1969), combined with EDS (Russ 1971), has also been used for decades to study elemental composition of minerals in geological samples (Krinsley and Margolis 1969; Jones, et al. 1981; Watt, et al. 2000; Reed 2005; Robinet, et al. 2015). It is a flexible tool that can be used to obtain detailed two dimensional information on the pore space of a sample with a resolution approaching 0.1 μm (Sardini, et al. 2006) as well as to identify elements and minerals via elemental mapping, but its limited field of view restricts its suitability for large samples (Sardini, et al. 1999). SEM-EDS is most useful when combined with methods more suitable for larger samples, such as X-ray microtomography (Voutilainen, et al. 2013) and the ^{14}C-PMMA autoradiography technique (Cassiaux, et al. 2006; Leskinen, et al. 2007; Sammaljärvi, et al. 2017). SEM-EDS imaging can be enhanced using contrast agents to highlight features. Wood’s metal is an alloy of different metals that has a low melting point (70 °C), which is an often used contrast agent to highlight pore space in variety of materials (Abell, et al., 1999; Hildenbrand & Urai, 2003; Kaufmann, 2009; Desbois et al., 2016). Wood’s metal also has good X-ray attenuation coefficient which is why it has also been used as a contrast agent in X-ray tomography (Pyrak-Nolte, et al., 1995; Pyrak-Nolte, et al., 1997). Wood’s metal has been reported to intrude at least 10 nm size pores (Klaver, et al., 2015) and 4.1 nm pore sizes have been reported as well (Desbois, et al., 2016). This however can still leave notable amount of pore space unfilled, if there are mineral phases with very small pore sizes. Wood’s metal intrusion is also a pressure-driven process and this can be a cause of artefacts

(Klaver, et al., 2015). Therefore, our first goal was to set out to investigate another type of contrast agent for both X-ray tomography and SEM-EDS without the necessity of pressure-driven intrusion.

Diffusion and sorption in crystalline rock are well known in large scales and on a molecular level, but in micrometre scale there are still many uncertainties that have led to conscious underestimation of the retarding capacity of the bedrock in applications such as the safety assessment of a nuclear waste depository (Posiva Oy 2013). It has also been shown that the heterogeneity of the rock structure and mineralogy can have a significant effect on the observed transport properties (Voutilainen, et al. 2013: Muuri, et al. 2016). A second goal of the study was to highlight the migration routes within the crystalline rock using a contrast agent.

The samples were chosen with two in-situ transport experiments in mind, Water Phase Diffusion Experiment (WPDE), an advection-matrix diffusion experiment being conducted under the “rock matrix REtention PROperties” (REPRO) project (Aalto, et al. 2009; Voutilainen, et al. 2014) in the REPRO-niche (Toropainen 2012) in ONKALO, Olkiluoto, Finland and Long Term Diffusion experiment (LTD) (Soler, et al. 2015), another matrix diffusion experiment, which was conducted at the Grimsel test site, Switzerland. Thus we chose to investigate Olkiluoto veined gneiss and Grimsel granodiorite. The Grimsel in-situ experiment, as well as an in-situ Through Diffusion Experiment (TDE) in Olkiluoto, have used caesium as a tracer in concentrations resembling the repository conditions. Results of caesium from the LTD experiment indicate that the mineral heterogeneity of the rock is important for retention of caesium (Jokelainen, et al. 2013; Voutilainen, et al. 2017). This factor combined with the high X-ray attenuation coefficient of caesium, and the possibility of facile intrusion via water solution, led to the decision to choose CsCl as the potential contrast agent. In order to test the feasibility of detecting caesium phase at all, saturated solution was used. Three samples of each rock type were investigated with computed X-ray microtomography and SEM-EDS.

2. MATERIALS AND EXPERIMENTAL METHODS

2.1. Samples

Olkiluoto bedrock was formed 1.80-1.91 billion years ago by the deformation and metamorphosis of supracrustal, metasedimentary and metavolcanic rocks (Kärki & Paulamäki 2006). On the other hand the Grimsel bedrock is only about 0.03-0.30 billion years old and has undergone transformations after that as well (Kralik, et al. 1992). Thus there is a sharp contrast in the ages of the bedrock in the two sites.

Veined gneiss is one of the main rock types in Olkiluoto bedrock around the ONKALO site. The samples for this study are taken from about 400 m deep within the bedrock (Toropainen 2012). The Olkiluoto veined gneiss contains migmatites with vein-like, elongated leucosomes (Kärki & Paulamäki 2006). A typical porosity value for Olkiluoto veined gneiss from experimental site of REPRO project is around 0.73 % (Ikonen, et al., 2015). SEM imaging revealed open unfilled pores mostly in the range of a few micrometres in the Olkiluoto veined gneiss (Sammaljärvi, et al., 2017). Recent studies applying C-14-PMMA autoradiography have shown that there are considerable amount of nanometre scale pores and their contribution to transport by diffusion can be considered remarkable (Sammaljärvi, et al., 2017; Kuva, et al., 2016). The main minerals of Olkiluoto veined gneiss are biotite (~30 %), quartz (~30 %), potassium feldspar (~15 %) and plagioclase (~15 %). Common accessory minerals are muscovite, chlorite, cordierite (often pinitised), sillimanite, epidote, garnet and opaque minerals (~10 % total). Interlamellar space of biotite is often filled with kaolinite, chlorite and illite, and clay minerals are found in pinitised cordierites as well (Sammaljärvi, et al. 2017). This, along with the random nature of the leucosome veins, means that the rock is very heterogeneous and anisotropic from microscopic to decametre scales (Aaltonen, et al. 2016; Ikonen, et al. 2015).

Grimsel Test Site on the other hand is located in the Swiss Alps and lies at a depth of about 450 m below the ground surface. Grimsel bedrock around the Grimsel Test Site consists of Grimsel

granodiorite and Aare granite. A typical porosity value for Grimsel granodiorite is around 0.5-1.0 % (Ikonen et al., 2016, Möri et al., 2003). Various analyses done previously on Grimsel granodiorite by SEM found grain boundaries and pores also in the range of a few micrometres (Möri, et al., 2003; Kelokaski, et al., 2006) but the mean pore diameter as measured by Hg-porosimetry was found to be in the nanometre range (Kelokaski, et al., 2006). Furthermore, recent studies applying C-14-PMMA autoradiography have shown that mineral grains with intra granular nanometre scale pores (e.g. biotite) affect considerably the transport of radionuclides (Voutilainen, et al., 2017). The main minerals of Grimsel granodiorite, which was used in this work, are quartz (~35 %), plagioclase (~30 %), potassium feldspar (~30 %) and biotite (~5 %). Minor constituents include muscovite, chlorite, epidote, allanite, zircon and apatite (Alexander, et al. 1990; Frick, et al. 1992). The biotite and clay mineral content is an important quality, as the sorption of cations is known to be significantly higher in biotite and clays than in other non-altered main minerals of crystalline rock (Ittner, et al. 1990; Tsukamoto and Ohe 1993; Jokelainen, et al. 2013). Caesium sorption has been studied in both rock types using lower caesium concentration than here and these studies have shown high sorption on biotite, although clay minerals also contributed to the sorption (Muuri, et al. 2016; 2017).

From both rock types described above three cubic samples (1·1·1 cm^3), six in total, were sawn (see Fig. 1). The samples were taken close to each other to ensure they had roughly similar composition and structure. Olkiluoto veined gneiss samples were taken from drill core ONK-PP323 in REPRO niche (Ikonen, et al. 2015) and Grimsel granodiorite samples from LTD monopole 1 drill hole in AU gallery at Grimsel test site (Ikonen, et al. 2016). Five of the six faces of the samples were sealed with an epoxy resin to allow CsCl to intrude the sample from only one side. For each sample the face opposite to the open one was attached to a sample holder for microtomographic imaging.

Figure 1. One sample from both rock types, Olkiluoto veined gneiss on the left and Grimsel granodiorite on the right, prepared for X-ray microtomography. Sample size is 1·1·1 cm^3.

2.2. X-ray microtomography

Computed X-ray microtomography is a method where, by detecting the difference in X-ray attenuation between different parts of a sample, three dimensional images of a sample are produced non-invasively. The sample is rotated with small increments and a two dimensional projection is taken at each step. The projections, of which a few hundred to a few thousand are usually taken, can then be computationally reconstructed into a three dimensional X-ray attenuation map. As the X-ray attenuation coefficient of a material is generally proportional to the elemental composition and density of the sample, this can also be interpreted as a three dimensional density map.

The microtomographic images used in this work were obtained with a SkyScan 1172 (Bruker microCT, Kontich, Belgium) table top scanner, which has a tungsten anode X-ray tube with polychromatic spectra and conical X-ray beam. They were imaged with a 6.1 μm voxel size using a source voltage of 100 kV and a source current of 80 μA. In order to reduce beam hardening, X-rays with low energy were filtered out from X-ray spectra using aluminium and copper filters. After this treatment the maximum intensity of spectra is at 59 keV (Kα energy of tungsten) and the theoretical maximum energy is 100 keV. The samples were scanned over a 203.8 degree rotation with a 0.2 degree rotation step, resulting in a total of 1020 projections. Each projection was averaged over 10 exposures of 6479 ms and the total scanning time was roughly 20 hours. The images were reconstructed with the SkyScan NRecon software using a ring artefact correction setting of 6-12 and beam hardening correction of 45-50 %. NRecon software applies Feldkamp algorithm (Feldkamp et al., 1984) for reconstruction and has an in-built alignment tool that is based on comparison of two projections taken from opposite directions.

The resolution of X-ray microtomography is 6.1 μm, and the majority of the pores in Grimsel granodiorite and Olkiluoto veined gneiss remain undetected. It is however expected that caesium chloride increases a local X-ray attenuation which is a parameter that is averaged over the volume of each voxel. On the other hand, pores within the mineral grain decrease the local X-ray attenuation, but often in natural materials the decrease is lost due to noise of signal and thus comparison of images taken before and after intrusion experiment is needed.

2.3. Scanning electron microscopy

The samples were carbon coated for the analyses and the analyses were performed using a field emission scanning electron microscope (FE-SEM) JEOL JSM 7100F Schottky (JEOL, Tokyo, Japan), attached to an Oxford Instruments energy dispersive spectrometer (EDS) X-max 80 mm^2 and Hitachi S-4800 (Hitachi, Tokyo, Japan) model with Oxford instruments X-sight X-ray diffractometer. The energy resolution of the EDS detectors used is about 130 eV for Mn Ka with processing capabilities multichannel analyser with 2048 channels at 10 eV/ch The FE-SEM-EDS systems were operated by Oxford Instruments INCA and AZtec softwares. The analytical data obtained was semiquantitative and the sum of the components was normalized to 100 %. Typical detection limits in point analysis for different elements range between 0.3-0.5 wt%. For caesium the detection limit is 0.4 wt%. The FE-SEM-EDS was used in high vacuum mode with COMPO back scattered signal, 20 kV accelerating voltage and 1 nA probe current. . Elemental distribution maps were generated over the sections with Aztec with a montage technique that combines several individual high-resolution elemental maps and back scattered electron (BSE) images together.

2.4. CsCl intrusion experiments

All six samples were first imaged with X-ray microtomography and then submerged in a saturated CsCl solution. It was assumed that CsCl or caesium, if concentrated enough, could be detected using X-ray microtomography due to its high density (high X-ray attenuation) in the connected pore space of the rock samples. The precipitate might alter the transport pathways and even block some

pores but the result would probably only be reduced connectivity and increased tortuosity (Noiriel, et al., 2016). All samples remained submerged in saturated CsCl solution for 141 days, after which one sample of each type was imaged again with X-ray microtomography. The next two samples were imaged after 249 days of immersion and the final two samples after 365 days of immersion.

For image analysis the microtomographic three dimensional images taken before and after immersion in saturated CsCl solution, had to be perfectly aligned. This was done with an in-house program that required the user to identify three features from the first image and the same three features from the second image. These features were mainly small grains of high density minerals, roughly 5·5·5 voxels in size, of which the middle voxel was identified as the feature. The program then defined the Euclidean transform that matches the features optimally and used this transform to align the images.

The samples that had been submerged for 141 days were dried and then impregnated with methyl methacrylate (MMA) which was subsequently polymerized to polymethylmethcrylate (PMMA) to fix the caesium phases into the pore space. This step is necessary as CsCl is a water-soluble compound which could be washed away during the sample handling. MMA is expected to fill any space left vacant by the contrast agent and also intrude into the pores within the CsCl precipitate itself. As MMA is a hydrophobic compound, it is not expected to dissolve the CsCl precipitate. There is however possibility that the polymerization heat and the contraction of MMA as it polymerizes could affect the CsCl precipitate. The MMA is however diluted by the rock matrix and there is only small volume of MMA in any given volume, dampening the possible effects of the polymerisation process. This process has also been found to work for celestite precipitated into compacted illite (Chagneau, et al., 2015). After the polymerization, these two samples were then sawn in half, polished, carbon coated and investigated with SEM-EDS. An illustration of the different steps in the transport experiment is shown in Fig. 2.

Figure 2. Illustration of the different steps of the experiment. Samples were first imaged with microtomography, then immersed in a saturated CsCl solution for 141, 249 and 365 days, then imaged with microtomography and SEM-EDS.

3. RESULTS

3.1. X-ray microtomographic imaging

All six samples were imaged with X-ray microtomography before and after immersion to a saturated CsCl solution. Cross-sections of the three dimensional microtomographic images (one representative slice was chosen for each sample), as well as the images showing the difference between the pre- and post-immersion images, are shown in Figs. 3-4. The main minerals are the same in both rock types. In pre-immersion images the main minerals are seen as light grey (biotite), intermediate grey (potassium feldspar and plagioclase) and dark grey (quartz). Some accessory minerals are seen as white spots and other might overlap with the grey values of the main minerals. In post-immersion images the new areas with increased grey value show location of CsCl as it is heavier than the main elements in the minerals. In the images showing the difference between pre- and post-immersion images the change in attenuation of X-rays and location of caesium is even more pronounced. It is clearly visible that Olkiluoto veined gneiss contains more biotite which is an iron rich mineral and denser than feldspars and quartz. In both sample types the foliation is shown in the images. It is more pronounced in veined gneiss in this scale, which has smaller grain size than Grimsel granodiorite. It can also be seen that the orientation of the minerals varies from sample to sample. It is parallel to CsCl intrusion in most samples, but perpendicular to it in one sample from both sites.

Figure 3. Microtomographic cross-sections of the Olkiluoto veined gneiss samples immersed in the saturated CsCl solution for 141 days (top row), 249 days (middle row) and 365 days (bottom row) taken before (left column) and after (middle column) the saturated CsCl solution immersion, along with a difference of the two (right column). A lighter grayscale value indicates a denser mineral. The CsCl solution intrusion surface is the upper edge. Sample width is 1 cm.

Figure 4. Microtomographic cross-sections of the Grimsel granodiorite samples immersed in the saturated CsCl solution for 141 days (top row), 249 days (middle row) and 365 days (bottom row) taken before (left column) and after (middle column) saturated CsCl solution immersion, along with a difference of the two (right column). A lighter grayscale value indicates a denser mineral. The CsCl solution intrusion surface is the upper edge. Sample width is 1 cm.

It is evident that there is very little CsCl intrusion in Grimsel granodiorite, as the quantities observed are small (see Fig. 4.). According to qualitative inspection of cross-sections show that increase in attenuation of X-rays due to accumulation of caesium are mainly located in biotite areas. In Grimsel granodiorite a slightly higher porosity has been observed for biotite than the rest of the minerals.

In Olkiluoto veined gneiss there is intrusion of CsCl throughout the samples in large quantities (see Fig. 3.). Qualitative inspection showed that the highest changes in attenuation of the X-rays are located at intermediate grey areas. These areas should not have high porosities or large pore apertures since they should be represent the potassium feldspar and plagioclase. However, Olkiluoto veined gneiss contains cordierite grains (6.6 vol-%) which are known to have relatively high porosities if they have experienced alteration to pinite (Ikonen, et al., 2015; Sammaljärvi, et al., 2017). In order to resolve the mineral phase of the areas with large changes in attenuation of X-rays SEM-EDS –analyses were performed. It is noteworthy that almost no pores or fissures can be

seen in the images, as the apertures are mostly below the 6.1 μm resolution used. The CsCl does, however, reveal many pores and areas of high local porosity which was the main aim of this study.

3.2. Analysis of the microtomographic images

In an attempt to quantify the amount of CsCl and pure caesium in the samples and the intrusion profiles, Z-profiles of the difference images in Figs. 3-4 were determined. This was done by taking an average grayscale value for each horizontal voxel plane from the intrusion surface to the bottom of the sample in the three dimensional image. Thus we could obtain a dimensionless estimate for the amount of caesium in the samples as a function of distance from the intrusion face, which is shown in Fig. 5. This makes the difference in caesium infiltration between the two rock types even clearer. There is much more caesium in the Olkiluoto veined gneiss samples. In fact, the Olkiluoto veined gneiss samples are completely saturated with all diffusion times, even when the foliation has been perpendicular to the intrusion (365 days). This can be seen by the overlapping of the curves and a lack of slope inside the sample. The variation seen in the Z-profiles is due to the varying contents of minerals, as a function of distance from the intrusion face. The high values at the intrusion surface are due to caesium precipitated on the sample surface. The Grimsel granodiorite samples seem to be saturated too, but they lack the high porosity mineral clusters that act as CsCl sinks in Olkiluoto veined gneiss. The difference in pore structures can already be seen by comparing previous C-14-PMMA autoradiography studies of the two rock types (Kelokaski, et al. 2006; Ikonen, et al. 2015). As there is no change as a function of time, no information on intrusion rate could be obtained. The differences in the profiles of the Olkiluoto veined gneiss samples can be attributed to the differences between the samples themselves.

Figure 5. Z-profiles of microtomographic images depicting the change in the Olkiluoto veined gneiss (left panel) and the Grimsel granodiorite (right panel) samples caused by immersion into the

315 saturated CsCl solution. Much more significant caesium intrusion can be seen in the Olkiluoto
316 veined gneiss samples than the Grimsel granodiorite samples. The profiles peak at ~5000 for
317 Grimsel granodiorite and ~3000 for Olkiluoto veined gneiss.

318 The grayscale changes were also investigated from each sample by comparing the grayscale values
319 of single voxels from pre-immersion images to the grayscale values of corresponding voxels in the
320 post-immersion images. The images were converted from 16 bits to 8 bits with a linear conversion
321 for this analysis. The loss of grayscale data resolution was deemed acceptable as the comparison
322 was mainly qualitative in nature. The contour plots obtained this way can be seen in Figs. 6-7. In an
323 ideal case with no caesium intrusion these plots would just have a sharp ridge at the $x=y$ line. Any
324 caesium intrusion increases the grayscale value of a voxel and is then seen as a shift towards the
325 positive *y*-axis. In the Olkiluoto veined gneiss samples (Fig. 6) there is a clear shift of the first
326 grayscale peak, located between grayscale values 50-100. This peak contains mainly quartz and
327 feldspars, which can be visually separated from a microtomographic image but are too similar to be
328 quantitatively distinguished (which has already been shown by Boone, et al. 2011 and Kuva, et al.
329 2012), and the other less pronounced peak located between grayscale values 125-150 contains
330 biotite. In the Grimsel granodiorite samples (Fig. 7) the intruded caesium can be seen as a slight
331 shift of the profile towards the positive *y*-axis for all the minerals which is in line with the previous
332 finding that the porosity of different minerals in Grimsel granodiorite are fairly close to each other.

333

334 Figure 6. Comparisons of grayscale values (8 bit) of voxels before the immersion into the saturated
335 CsCl solution and the grayscale values of the corresponding voxels after the immersion into the
336 saturated CsCl solution for Olkiluoto veined gneiss samples immersed for 141 days (left panel), 249
337 days (middle panel) and 365 days (right panel). The colours describes the amount of voxels. A clear
338 shift in the peak located between values 50-100 can be seen on each image. A smaller shift is also
339 seen in the peak located between values 125-150, indicating some retention of caesium.

Figure 7. Comparisons of grayscale values (8 bit) of voxels before the immersion into the saturated CsCl solution and the grayscale values of the corresponding voxels after the immersion into the saturated CsCl solution for Grimsel granodiorite samples immersed for 141 days (left panel), 249 days (middle panel) and 365 days (right panel). The colours describes the amount of voxels. A small shift towards the positive *y*-axis is seen for all minerals.

3.3. SEM-EDS Analysis

The PMMA impregnated samples were analysed with SEM-EDS to see the location and content of CsCl in respect to different minerals. Only very little caesium was found in the Grimsel granodiorite sample and all of the caesium was as pure precipitated CsCl in micrometre scale pores. These pores with pure precipitate were, however, found throughout the whole sample which proves that the precipitate has not blocked up the migration routes in the Grimsel granodiorite. Furthermore, it can be assumed according to the data shown in Figs. 5 and 7 that there might be elevated concentration of caesium in some minerals having the pores below micrometre scale but the amount is below the detection limit of the SEM-EDS (<0.4 wt%).

In the Olkiluoto veined gneiss sample, a significant amount of caesium was found using SEM-EDS. Examples of caesium findings by SEM-EDS are shown in Fig. 8. In some cases intragranular pores and fissures contained precipitated CsCl. The CsCl precipitates were found in different shapes and sizes as can be seen in the Fig. 8. In Olkiluoto veined gneiss the largest quantities of caesium were found in pinitised areas of cordierite grains. Pinite is an alteration product of cordierite with a varying composition which can include muscovite, chlorite, berthierine, illite and smectite in various ratios and interlayers (Ogiermann, 2002). In Fig. 8. an example of such a location is shown with a pinitised cordierite grain, sphalerite, zircon inclusions, a biotite grain and a fractured quartz grain. Here caesium was also found in sphalerite, wherein no chloride was

detected. Another example of pinitised cordierite containing caesium and chloride, together with biotite and muscovite, is also shown. In the pinitised grains caesium was found in considerable excess compared to chloride. In some areas of particularly high caesium abundance no chloride could be reliably detected. All in all, both caesium and chloride were found in pinitised cordierite in differing abundances and ratios. In CsCl itself the atomic ratio of caesium to chloride is 1. However, in pinite this ratio ranged from 2.0 to 6.2 (see Table 1.). Chloride was not always detected together with caesium in the point analyses. In addition, a biotite grain with a kaolinite-filled interlamellar space near the edge of the sample is shown in Fig. 8. Caesium was found in parity ratio with chloride in the kaolinite-filled interlamellar space. Furthermore, in this case caesium chloride was also found in a 10 µm wide band in biotite starting from the edge of the original CsCl intrusion, along with chloride.

Figure 8. SEM BSE images. Upper left: Quartz (Q) grains with CsCl precipitate in its intragranular fissure. Upper right: Fractured quartz grain, intact biotite (BT) lamellae and partially pinitised cordierite (CRD) grain. Small grains of sphalerite (SP) and Zircon (ZRN). Caesium and chloride found in pinite (PI) and high content of caesium found in sphalerite. Lower left: Biotite lamellae from the edge of the sample and interlamellar pores filled with kaolinite (KLN). Caesium and chloride found in parity abundance in kaolinite. Caesium, along with chloride, found in large abundance in a 10 µm deep area in the disturbed biotite. Lower right: Highly pinitised cordierite grain adjacent to biotite and muscovite (MU). Large abundances of caesium and some chloride were found in the pinite with their abundance correlating directly with the level of pinitisation.

Summary of caesium and chloride abundances and their ratios are shown in Table 1. A large range of values where found in pinite. There was a direct correlation of retention of caesium with the level of pinitisation. In kaolinite the retention was lower but still notable and the range of values was narrower. Retention of caesium on sphalerite grains was considerable, while chloride retention was

not observed. Sphalerite is not, however, a common mineral in Olkiluoto veined gneiss and therefore a range could not be established.

Table 1. Caesium and chloride abundances in atomic% and their ratios sorted by the minerals where they were found in notable amounts. The values given are averages with the ranges given in brackets. In few areas of pinite that had the highest caesium abundances, the chloride abundance could not be determined.

Elemental maps of caesium and chloride with corresponding BSE SEM image from a larger area of the Olkiluoto veined gneiss sample are shown in Fig. 9. It can be seen that caesium is found in high abundance with roughly similar amount chloride and in notable excess compared to chloride. In both cases caesium appears to reside in the porous spaces of the rock sample which, in the case of excessive abundance of caesium, were identified to be congruent with pinitised cordierite. There is background noise in the elemental maps due to the long measurement times involved. In the case of caesium, the titanium found in biotite can also interfere due to X-ray emissions with energies very similar to those of caesium.

Figure 9. BSE SEM image of a larger part of the Olkiluoto veined gneiss sample (left panel) along with an elemental map of caesium (middle panel) and chloride (right panel) from the same area, showing that some caesium patches are precipitated with roughly similar amount of chloride (examples marked with A) and other with less chloride (examples marked with B).

Finally, the Olkiluoto veined gneiss sample imaged with SEM-EDS was imaged again with X-ray microtomography. This was done to find the surface corresponding to the SEM images

412 from the microtomographic image significantly easier and to make sure that if the MMA-
413 impregnation caused any changes in the caesium inside the sample, the same changes would be
414 present in the microtomographic image. The surface corresponding to the SEM images was then
415 located from the microtomographic image. This surface, shown along with a difference image
416 compared to the original microtomographic image of the same sample in Fig. 10, shows that CsCl
417 could be detected with X-ray microtomography as well in corresponding locations and concentrated
418 caesium was observed in pinitised cordierites. According to SEM-EDS analyses these locations
419 contained from 1.1 to 8.0 atomic% of caesium which leads to a finding that such abundances can be
420 easily detected with X-ray microtomography when using the different methods.

421

422 Figure 10. X-ray microtomographic cross-section of a Olkiluoto veined gneiss sample with an area
423 corresponding with that of Fig. 9 (left panel) and a corresponding difference image with the first
424 microtomographic imaging of the same sample, showing CsCl in connected pore space and
425 concentrated caesium in pinitised cordierite grains. A and B areas correspond to the marked areas in
426 Fig.9.

427 **4. DISCUSSION and CONCLUSIONS**

428 The primary objective of this work was to test if connected porosity within crystalline rock could be
429 seen using CsCl as a contrast agent. This objective was achieved as it was found that CsCl enhanced
430 the local X-ray attenuation so that connected porosity Olkiluoto veined gneiss and Grimsel
431 granodiorite, to a lesser extent, could be imaged.

432 The two rock types are different in their mineralogy and the structure of the pore network,
433 which was seen in the results. Much more significant caesium intrusion was seen in Olkiluoto
434 veined gneiss than Grimsel granodiorite, despite earlier studies showing Grimsel granodiorite to be
435 more conductive than Olkiluoto veined gneiss (Kelokaski, et al. 2006; Kuva, et al. 2015). In

Olkiluoto veined gneiss there are more areas of high local porosity congruent with cordierites and its alteration product pinite where CsCl was accumulated. These highly porous areas were more easily distinguished with the improved contrast using the SEM-EDS and X-ray microtomography. No clear time dependence on the intrusion depth was detected, which likely means that all samples were already saturated after 141 days of immersion and thus no information on intrusion rate was obtained. Complete infiltration of the CsCl into the Olkiluoto veined gneiss samples showed that connected transport pathways remained open despite the CsCl precipitation in the pore openings. Presence of micrometre scale pores may have caused the complete infiltration of CsCl in relatively short time. However, previous studies have shown that porosity of these samples has considerable contribution from nanometre scale pores and thus their contribution cannot be neglected.

Closer investigation of the microtomographic images showed that in Olkiluoto veined gneiss the CsCl precipitates were found most extensively in cordierite grains and in some extent in pinitised cordierite grains. This is expected as the most pronounced effect is coming from the caesium that is accumulated in the pore space of the rock, since the cation exchange capacity of biotite and studied rock samples is relatively low considering the effect it can have on the local attenuation coefficient (Olin, et al. 2006; Muuri, et al. 2016; 2017). In Grimsel granodiorite the density change was smaller and took place relatively evenly in all minerals. The results by X-ray microtomography were supplemented and verified using SEM-EDS analyses which showed that both sample types had precipitated CsCl in the micrometre scale pores throughout the sample. The CsCl precipitates came in a variety of shapes and sizes. This is probably due to the sample drying before the impregnation and the PMMA impregnation procedure itself, which could disrupt the precipitate structure. However without the PMMA impregnation procedure, the precipitate would likely be washed off during the SEM-EDS sample preparation. Not all fissures were found to be filled with CsCl. Some of the fissures however can have come about after the immersion with the CsCl solution as the result of the sample preparation (Schild, et al., 2001). Similar procedure has

been done on compacted illite wherein celestite was precipitated into the pores structure and similar-looking structures were obtained (Chagneau, et al., 2015). In the Olkiluoto veined gneiss the highest abundances of CsCl were found in pinitised cordierite, with other notable locations of high caesium abundance being the kaolinite-filled interlamellar space of biotite and on sphalerite. In biotite itself caesium was found in notable amounts in the disturbed edge zone. In the elemental mapping of Fig 9. In pinite caesium was found in notable excess compared to chloride. The excess of caesium compared to chloride in pinite indicates that caesium experiences more retention in pinite than chloride. In some points, no chloride could be detected at all. These points corresponded mostly with areas of pinite where highest amounts of caesium where found. It is likely that these points corresponded to fine-grained clay minerals where chloride is not able to enter in detectable amounts due to possible anion exclusion. This causes the effective porosity for cations to be significantly higher than the effective porosity for anions (Smith, et al., 2004). Anion exclusion has been shown to be comparatively high in smectite and illite, but less so in kaolinite (Glaus, et al., 2010). This could explain why caesium was found in excess compared to chloride only in pinite but not in the interlamellar kaolinite. Anion exclusion is usually not complete, unless special measures, such as clogging pores with celestite beforehand are used (Chagneau, et al., 2015). As no such treatment preceded the CsCl-immersion, chloride was usually found also in pinite, in small, sub parity quantities. Caesium is, however, also a strong sorber on edge sites of illite, which may also contribute to its strong retention in pinite, even though saturation concentration used in this work is not ideal for sorption (Wahlberg & Fishman, 1962). Future experiment with water and anionic tracers will be done to clarify the mechanisms behind the observed results. Comparison to microtomographic images of the same sample confirmed that the same areas could be distinguished with microtomography. In the Grimsel granodiorite samples the caesium was found only as precipitated CsCl in a few connected pore apertures. This effect certainly arose from the differences in mineral and pore structures.

Based on the results obtained it can be said that X-ray microtomography is a capable tool in investigating transport pathways in tight crystalline rock when combined with a suitable contrast agent. The results can be enhanced and complemented with SEM-EDS. Looking beyond the results obtained in this study, the methods applied here could be: (1) used in an experiment with shorter immersion times to obtain information on intrusion speed, (2) further developed by applying autoradiography to provide complementary imaging for spatial activity distribution with a radioactive contrast agent, and (3) applied to provide spatial distribution of the elements used in in situ-diffusion experiments such as LTD and TDE.

6. REFERENCES

Aalto, P., et al. (2009) *Programme for repository host rock characterisation in the ONKALO (ReRoC).* Working Report 2009-31, Posiva Oy.

Aaltonen, I. (ed.), et al. (2016) *Geology of Olkiluoto*, POSIVA report 2016-16, Posiva Oy.

Abell, A.B., Willis, K.L. & Lange, D.A. (1999) *Mercury intrusion porosimetry and image analysis of cement-based materials.* J. Colloid Interface Sci. 211, 39-44.

Alexander, W. R., MacKenzie, A. B., Scott, R. D. & McKinley, I. G. (1990) *Natural analogue studies in crystalline rock: The influence of water-bearing fractures on radionuclide immobilization in a granitic rock repository.* Technical Report NTB 87-08, Nagra.

Boone, M., et al. (2011) *Three-dimensional phase separation and identification in granite*. Geosphere 7, 79-86.

Bultreys, T., Boone, M. A., Boone, M. N., De Schryver, T., Masschaele, B., Van Hoorebeke, L. & Cnudde, V. (2016) *Fast laboratory-based micro-computed tomography for pore-scale research: Illustrative experiments and perspectives on the future.* Adv. in Water Resour. 95, 341-351.

508 Cassiaux, M., Proust, D., Siitari-Kauppi, M., Sardini, P. & Leutsch Y. (2006) *Clay minerals formed*
509 *during propylitic alteration of a granite and their influence on primary porosity: a multi-scale*
510 *approach.* Clay Miner. 54(5), 541-554.

511 Chagneau, A. et al. (2015) *Complete restriction of $^{36}Cl^-$ diffusion by celestite precipitation in*
512 *densely compacted illite.* Environ. Sci. Technol. Lett. 2, 139-143.

513 Cnudde, V. & Boone, M. N. (2013). *High-resolution X-ray computed tomography in geosciences: A*
514 *review of the current technology and applications.* Earth-Sci. Rev. 123, 1-17.

515 Cormack, A.M. (1963). *Representation of a function by its line integrals, with some radiological*
516 *applications.* J. Appl. Phys. 34, 2722-2727.

517 Desbois, G. et al. (2016) *Investigation of microstructures in naturally and experimentally deformed*
518 *reference clay rocks using innovative methods in scanning electron microscopy.* The Clay Minerals
519 Society Workshop Lectures Series, 21, 1-14.

520 Eastwood, D. S.et al. (2014) *Lithiation-induced dilation mapping in a lithium-ion battery electrode*
521 *by 3D X-ray microscopy and digital volume correlation.* Adv. Energy Mater. 4(4), 1300506.

522 Farber, L., Tardos, G. & Michaels, J. N. (2003). *Use of X-ray tomography to study the porosity and*
523 *morphology of granules.* Powder Technol. 132, 57-63.

524 Feldkamp, L.A., Davis, L.C., Kress, J.W. (1984) Practical conebeam algorithm. J. Opt. Soc. Am. A.
525 1(6), 612-619.

526 Frick, U. et al. (1992) *Grimsel Test Site: The radionuclide migration experiment – overview of*
527 *investigations 1985-1990.* Paul Scherrer Institute, Wettingen.

528 Fusseis, F., Xiao, X., Schrank, C. & De Carlo, F. (2014) *A brief guide to synchrotron radiation-*
529 *based microtomography in (structural) geology and rock mechanics.* J. Struct. Geol. 65, 1–16.

Glaus, M.A., Frick, S., Rossé, R. & Van Loon, L.R. (2010) *Comparative study of tracer diffusion of HTO, Na-22, Cl-36 in compacted kaolinite, illite and montmorillonite.* Geochim. Cosmochim. Acta 74, 1999-210.

Gommes, C. J., Bons, A.-J., Blacher, S., Dunsmuir, J. H. & Tsou, A. H. (2009) *Practical methods for measuring the tortuosity of porous materials from binary or gray-tone tomographic reconstructions.* AlChE Journal 55(8), 2000-2012.

Gouze, P. & Luquot, L. (2011) *X-ray microtomography characterization of porosity, permeability and reactive surface changes during dissolution.* J. Contam. Hy*drol.* 120-121, 45-55.

Hellmuth, K.-H., Siitari-Kauppi, M. & Lindberg, A. (1993). *Study of porosity and migration pathways in crystalline rock by impregnation with 14C-polymethylmethacrylate*. J. Contam. Hydrol. 13(1-4), 403-418.

Hildenbrand, A. & Urai, J.L. (2003) *Investigation of the morphology of pore space in mudstones – first results*. Mar. Pet. Geol. 20, 1185-1200.

Hoagland, R. G., Hahn, G. T. & Rosenfield, A. R. (1973) *Influence of Microstructure on Fracture Propagation in Rock.* Rock Mech. 5, 77-106.

Hounsfield, G. N. (1973) *Computerized transverse axial scanning (tomography): Part 1. Description of the system*. Brit. J. Radiol. 46, 1016-1022.

Ikonen, J., Sammaljärvi, J., Siitari-Kauppi, M., Voutilainen, M., Lindberg, A., Kuva, J. & Timonen, J. (2015) *Investigation of rock matrix retention properties. Supporting laboratory studies I: Mineralogy, porosity and pore structure*. Posiva Working Report 2014-68, Posiva Oy.

Ikonen, J., Sardini, P., Jokelainen, L., Siitari-Kauppi, M., Martin, A. & Eickenberg, J. (2016) *The tritiated water and iodine migration in situ in Grimsel granodiorite. Part I: determination of the diffusion profiles.* J. Radioanal. Nucl. Chem. 310, 1041-1048.

553 Ittner, T. & Torstenfeit, B., Allard, B. (1990) *Diffusion of Strontium, Technetium, Iodine and*
554 *Caesium in Granitic Rock*. Radiochim. Acta 49, 101-106.

555 Jacques, P. D., Nummer, A. R., Heck, R. J. & Machado, R. (2014) *The use of microtomography in*
556 *structural geology: A new methodology to analyse fault faces*. J. Struct. Geol. 66, 347–355.

557 Jokelainen, L., Meski, T., Lindberg, A., Soler, J., Siitari-Kauppi, M., Martin, A. & Eikenberg, J.
558 (2013) *The determination of 134Cs and 22Na diffusion profiles in granodiorite using gamma*
559 *spectroscopy*. J. Radioanal. Nucl. Chem. 295, 2153–2161.

560 Jones, D., Wilson, M. J. & McHardy, W. J. (1981) *Lichen weathering of rock-forming minerals:*
561 *application of scanning electron microscopy and microprobe analysis*. J. Microsc. 124(1), 95-104.

562 Kak, A.C. & Slanley, M. (2001) *Principles of Computed Tomography Imaging.* Society for
563 Industrial and Applied Mathematics, Philadelphia, Pennsylvania.

564 Kaufmann, J. (2009) *Characterization of pore space of cement-based materials by combined*
565 *mercury and Wood's metal intrusion*. J. Am. Ceram. Soc. 92(1), 209-216.

566 Kelokaski, M., Siitari-Kauppi, M., Sardini, P., Möri, A. & Hellmuth, K.-H. (2006) *Characterisation*
567 *of pore space geometry by ^{14}C-PMMA impregnation – development work for in situ studies.* J.
568 Geochem. Explor. 90, 45-52.

569 Ketcham, R. A. & Iturrino, G. J. (2005) *Nondestructive high-resolution visualization and*
570 *measurement of anisotropic effective porosity in complex lithologies using high-resolution X-ray*
571 *computed tomography*. J. Hydrol. 302, 92-106.

572 Klaver, J., Hemes, S., Houben, M., Desbois, G., Radi, Z. & Urai, J.L. (2015) *The connectivity of*
573 *pore space in mudstones: insights from high-pressure Wood's metal injection, BIB-SEM imaging*
574 *and mercury intrusion porosimetry*. Geofluids, 15 (4), 577-591.

575 Kralik, M., Clauer, N., Holnsteiner, R., Huemer, H. & Kappel, F. (1992) *Recurrent fault activity in*
576 *the Grimsel Test Site (GTS, Switzerland): revealed by Rb-Sr, K-Ar and tritium isotope techniques.* J.
577 Geol. Soc. London 149(2), 293-301.

578 Krinsley, D. & Margolis, S. (1969) *Section of Geological Sciences: A Study of Quartz and Sand*
579 *Grain Surface Textures with the Scanning Electron Microscope*. T. New York Acad. Sci. 31(5),
580 457-477.

581 Kuva, J., Siitari-Kauppi, M., Lindberg, A., Aaltonen, I., Turpeinen, T., Myllys, M. & Timonen, J.
582 (2012) *Microstructure, porosity and mineralogy around fractures in Olkiluoto bedrock*. Eng. Geol.
583 139-140, 28-37.

584 Kuva, J., Voutilainen, M., Kekäläinen, P., Siitari-Kauppi, M., Timonen, J. & Koskinen, L. (2015)
585 *Gas phase measurements of porosity, diffusion coefficient and permeability in rock samples from*
586 *Olkiluoto bedrock, Finland*. Transp. Porous Med. 107(1), 187-204.

587 Kuva, J., Voutilainen, M., Kekäläinen, P., Siitari-Kauppi, M., Timonen, J. & Koskinen, L. (2016)
588 *Gas phase measurements of matrix diffusion in rock samples from Olkiluoto bedrock, Finland*.
589 Transp. Porous Med. 115(1), 1-20.

590 Kärki, A. & Paulamäki, S. (2006) *Petrology of Olkiluoto*. Posiva Report 2006-02, Posiva Oy.

591 Leskinen A., Penttinen L., Siitari-Kauppi M., Alanso U., Garcia-Gutierrez M., Missana T. & Patelli
592 A. (2007) *Determination of granites' mineral specific porosities by PMMA method and*
593 *FESEM/EDAX*. MRS Proceedings 985, 599-604.

594 Lowe, T., Garwood, R. J., Simonsen, T. J., Bradley, R. S. & Withers, P. J. (2013) *Metamorphosis*
595 *revealed: time-lapse three-dimensional imaging inside a living chrysalis.* J. R. Soc. Interface 10,
596 20130304.

597 Maire, E. & Withers, P. J. (2014) *Quantitative X-ray tomography*. Int. Mater. Rev. 59(1), 1-43.

McWilliams, J. (1966). *The role of microstructure in the physical properties of rock. Testing techniques for rock mechanics*. ASTM International.

Mokso, R., Marone, F., Haberthür, D., Schittny, J. C., Mikuljan, G., Isenegger, A. & Stampanoni, M. (2011) *Following dynamic processes by X-ray tomographic microscopy with sub-second temporal resolution*. AIP Conf. Proc. 1365, 38-41.

Muuri, E. et al. (2016) *Behavior of Cs in Grimsel granodiorite: Sorption on main minerals and crushed rock*. Radiochim. Acta 104(8), 575-582.

Muuri, E., Siitari-Kauppi, M., Matara-aho, M., Ikonen, J., Lindberg, A., Qian, L. & Koskinen, L. (2017) *Caesium sorption and diffusion on crystalline rock: Olkiluoto case study*. J. Radioanal. Nucl. Chem. 311(1), 439-446.

Möri, A., et al. (2003). Grimsel Test Site Investigation Phase IV (1994-1996). The Nagra-JNC in situ study of safety relevant radionuclide retardation in fractured crystalline rock IV: The in situ study of matrix porosity in the vicinity of a water conducting fracture. Technical Report 00-08. Nagra, Wettingen (Switzerland). ISSN: 1015-2636.

Nixon, W. C. (1969) *Scanning electron microscopy*. Contemp. Phys. 10(1), 71-96.

Noiriel, C., Steefel, C.I., Yang, L. & Bernard, D. (2016) *Effects of pore-scale precipitation on permeability and flow*. Advances in Water Resources, 95. 125-137.

Ogiermann, J. C. (2002) *Cordierite and its retrograde breakdown products as monitors of fluid-rock interaction during retrograde path metamorphism: case studies in the Schwarzwald and the Bayerische Wald (Variscan belt Germany)*. Doctoral Dissertation, University of Heidelberg, Heidelberg.

Olin, M., Puukko, E., Puhakka, E., Lehikoinen, J., Lindberg, A. & Hakanen, M. (2006) *Sorption of nickel on biotite*. Research Report VTT-R-08046-06, VTT Oy.

621 Posiva Oy (2013) *Safety case for the disposal of spent nuclear fuel at Olkiluoto – Models and data*
622 *for the repository system 2012*. Posiva Report 2013-01, Posiva Oy.

623 Pyrak-Nolte, L.J., Montemagno, C.D., Yang, G., Cook, N.G.W &, Myer, L.R. (1995) *Three-*
624 *dimensional tomographic visualization of natural fracture networks and graph theory analysis of*
625 *the transport properties*. Int. Soc. Rock Mech. Proc., 855-859.

626 Pyrak-Nolte, L.J., Montemagno, C.D., Nolte, D.D. (1997) *Volumetric imaging of aperture*
627 *distributions in connectd fracture networks*. Geophys. Res. Lett., 24(18), 2343-2346.

628 Radon, J. (1917) Über die Bestimmung von Functionen durch ihre Integralwerte längs gewisser
629 Mannigfaltigkeiten. Berichte der Sächsischen Akademie der Wissenschaft 69, 262-277.

630 Reed, S. J. B. (2005) *Electron Microprobe Analysis and Scanning Electron Microscopy in Geology*.
631 Cambridge University Press, Cambridge, UK.

632 Robinet, J. C., Sardini, P., Siitari-Kauppi, M., Prêt, D. & Yven, B. (2015) *Upscaling the porosity of*
633 *the Callovo-Oxfordian mudstone from the pore scale to the formation scale; insights from the 3H-*
634 *PMMA autoradiography technique and SEM BSE imaging*. Sediment. Geol. 321, 1-10.

635 Russ, J. C. (1971) *Energy dispersion x-ray analysis: x-ray and electron probe analysis*. 73rd annual
636 meeting of the American Society for Testing and Materials, Toronto, Ontario.

637 Sammaljärvi, J. et al. (2017) *Multi-scale study of the mineral porosity of veined gneiss and*
638 *pegmatitic granite from Olkiluoto, Western Finland*. Submitted for publication.

639 Sardini, P., Sammartino, S., Meunier, A. & Tévissen, E. (1999) *Evolution of fluid pathways of*
640 *Charroux-Civray tonalite (part II): Numerical study of microcrack networks*. Phys. Chem. Earth Pt
641 A 24(7), 621-625.

642 Sardini, P., Siitari-Kauppi, M., Beaufort, D. & Hellmuth, K.-H. (2006) *On the connected porosity of*
643 *mineral aggregates in crystalline rocks*. Am. Mineral. 91, 1069-1080.

644 Schild, M., Siegesmund, S., Vollbrecht, A., Mazurek, M. (2001) Characterization of granite matrix
645 porosity and pore-space geometry by in situ and laboratory methods. Geophys. J. Int. 146, 111-125.

646 Singh, K., Niven, R. K., Senden, T. J., Turner, M. L., Sheppard, A. P., Middleton, J. P. &
647 Knackstedt, M. A. (2011). *Remobilization of residual non-aqueous phase liquid in porous media by*
648 *freeze – thaw cycles*. Environ. Sci. Technol. 45, 3473-3478.

649 Smith, D., Pivonka, P., Jungnickel, C., Fityus, S. (2004) *Theoretical analysis of anion exclusion and*
650 *diffusive transport through platy-clay soils.* Transport Porous Med. 57. 251-277.

651 Soler, J. M., et al. (2015) *Comparative modeling of an in situ diffusion experiment in granite at the*
652 *Grimsel Test Site*. J. Contam. Hydrol. 179, 89-101.

653 Stock, S.R. (2009) *Microcomputed Tomography: Methodology and Applications*. CRC Press, Boca
654 Raton, Florida.

655 Thiemeyer, N., Habersetzer, J., Peinl, M., Zulauf, G. &Hammer, J. (2015) *The application of high*
656 *resolution X-ray computed tomography on naturally deformed rock salt: Multi-scale investigations*
657 *of the structural inventory*. J. Struct. Geol. 77, 92-106.

658 Thovert, J.-F., Yousefian, F., Spanne, P., Jacquin, C. G. & Adler, P. M. (2001) *Grain*
659 *reconstruction of porous media: Application to a low-porosity Fontainebleau sandstone.* Phys. rev.
660 E 63(6), 061307.

661 Toropainen, V. (2012) *Core drilling of REPRO drillholes in ONKALO at Olkiluoto 2010-2011*.
662 Posiva Working Report 2012-26, Posiva Oy.

663 Tsukamoto, M. & Ohe, T. (1993) *Effects of biotite distribution on caesium diffusion in granite*.
664 Chem. Geol. 107, 29-46.

665 Vernon, R.H. (2004) *A Practical Guide to Rock Microstructure*. Cambridge University Press,
666 Cambridge.

667 Voutilainen, M., Siitari-Kauppi, M., Sardini, P., Lindberg, A. & Timonen, J. (2012) *Pore-space*
668 *characterization of an altered tonalite by X-ray computed microtomography and the ^{14}C-labeled-*
669 *polymethylmethacrylate method*. J. Geophys. Res. 117, B01201.

670 Voutilainen, M., Sardini, P., Siitari-Kauppi, M., Kekäläinen, P., Aho, V., Myllys, M. & Timonen, J.
671 (2013) *Simulated diffusion of tracer in altered tonalite with heterogeneous distribution of porosity*.
672 Transp. Porous Med. 96(2), 319–336.

673 Voutilainen, M. et al. (2014*) In-situ experiments for investigating the retention properties of rock*
674 *matrix in ONKALO, Olkiluoto, Finland*. WM 2014 Conference Proceedings 40, WM, 14258.

675 Voutilainen, M., Kekäläinen, P., Siitari-Kauppi, M., Sardini, P., Muuri, E., Timonen, J., Martin, A.
676 (2017) *Modeling transport of cesium in Grimsel granodiorite with micrometer scale heterogeneities*
677 *and dynamic update of K_d*. Water Resour. Res., In press.

678 Wahlberg, J.S. & Fishman, M.J. (1962). Adsorption of Cesium on Clay Minerals. Geological
679 Survey Bulletin 1140-A. United States Government Printing Office, Washington. 1962 O-643872

680 Watt, G. R., Griffin, B. J. & Kinny, P. D. (2000) *Charge contrast imaging of geological materials*
681 *in the environmental scanning electron microscope*. Am. Mineral. 85(11-12), 1784-1794.

682 Wildenschild, D. & Sheppard, A. P. (2013) *X-ray imaging and analysis techniques for quantifying*
683 *pore-scale structure and processes in subsurface porous medium systems*. Adv. Water Resour. 51,
684 217-246.

685 Zabler, S., Rack, A., Manke, I., Thermann, K., Tiedemann, J., Harthill, N. & Riesemeier, H. (2008)
686 *High-resolution tomography of cracks, voids and micro-structure in greywacke and limestone*. J.
687 Struct. Geol. 30(7), 876-887.

688

689 **7. FIGURE & TABLE CAPTIONS**

690 Figure 1. One sample from both rock types, Olkiluoto veined gneiss on the left and Grimsel
691 granodiorite on the right, prepared for X-ray microtomography. Sample size is 1·1·1 cm^3.

692

693 Figure 2. Illustration of the different steps of the experiment. Samples were first imaged with
694 microtomography, then immersed in a saturated CsCl solution for 141, 249 and 365 days, then
695 imaged with microtomography and SEM-EDS.

696

697 Figure 3. Microtomographic cross-sections of the Olkiluoto veined gneiss samples immersed in the
698 saturated CsCl solution for 141 days (top row), 249 days (middle row) and 365 days (bottom row)
699 taken before (left column) and after (middle column) the saturated CsCl solution immersion, along
700 with a difference of the two (right column). A lighter grayscale value indicates a denser mineral.
701 The CsCl solution intrusion surface is the upper edge. Sample width is 1 cm.

702

703 Figure 4. Microtomographic cross-sections of the Grimsel granodiorite samples immersed in the
704 saturated CsCl solution for 141 days (top row), 249 days (middle row) and 365 days (bottom row)
705 taken before (left column) and after (middle column) saturated CsCl solution immersion, along with
706 a difference of the two (right column). A lighter grayscale value indicates a denser mineral. The
707 CsCl solution intrusion surface is the upper edge. Sample width is 1 cm.

708

709 Figure 5. Z-profiles of microtomographic images depicting the change in the Olkiluoto veined
710 gneiss (left panel) and the Grimsel granodiorite (right panel) samples caused by immersion into the
711 saturated CsCl solution. Much more significant caesium intrusion can be seen in the Olkiluoto

712 veined gneiss samples than the Grimsel granodiorite samples. The profiles peak at ~5000 for
713 Grimsel granodiorite and ~3000 for Olkiluoto veined gneiss.

714

715 Figure 6. Comparisons of grayscale values (8 bit) of voxels before the immersion into the saturated
716 CsCl solution and the grayscale values of the corresponding voxels after the immersion into the
717 saturated CsCl solution for Olkiluoto veined gneiss samples immersed for 141 days (left panel), 249
718 days (middle panel) and 365 days (right panel). The colours describes the amount of voxels. A clear
719 shift in the peak located between values 50-100 can be seen on each image. A smaller shift is also
720 seen in the peak located between values 125-150, indicating some retention of caesium.

721

722 Figure 7. Comparisons of grayscale values (8 bit) of voxels before the immersion into the saturated
723 CsCl solution and the grayscale values of the corresponding voxels after the immersion into the
724 saturated CsCl solution for Grimsel granodiorite samples immersed for 141 days (left panel), 249
725 days (middle panel) and 365 days (right panel). The colours describes the amount of voxels. A
726 small shift towards the positive *y*-axis is seen for all minerals.

727

728 Figure 8. SEM BSE images. Upper left: Quartz (Q) grains with CsCl precipitate in its intragranular
729 fissure. Upper right: Fractured quartz grain, intact biotite (BT) lamellae and partially pinitised
730 cordierite (CRD) grain. Small grains of sphalerite (SP) and Zircon (ZRN). Caesium and chloride
731 found in pinite (PI) and high content of caesium found in sphalerite. Lower left: Biotite lamellae
732 from the edge of the sample and interlamellar pores filled with kaolinite (KLN). Caesium and
733 chloride found in parity abundance in kaolinite. Caesium, along with chloride, found in large
734 abundance in a 10 μm deep area in the disturbed biotite. Lower right: Highly pinitised cordierite

735 grain adjacent to biotite and muscovite (MU). Large abundances of caesium and some chloride
736 were found in the pinite with their abundance correlating directly with the level of pinitisation.

737

738 Figure 9. BSE SEM image of a larger part of the Olkiluoto veined gneiss sample (left panel) along
739 with an elemental map of caesium (middle panel) and chloride (right panel) from the same area,
740 showing that some caesium patches are precipitated with roughly similar amount of chloride
741 (examples marked with A) and other with less chloride (examples marked with B).

742

743 Figure 10. X-ray microtomographic cross-section of a Olkiluoto veined gneiss sample with an area
744 corresponding with that of Fig. 9 (left panel) and a corresponding difference image (right panel)
745 with the first microtomographic imaging of the same sample, showing CsCl in connected pore
746 space and concentrated caesium in pinitised cordierite grains. A and B areas correspond to the
747 marked areas in Fig.9.

748

749 Table 1. Caesium and chloride abundances in atomic% and their ratios sorted by the minerals where
750 they were found in notable amounts. The values given are averages with the ranges given in
751 brackets. In few areas of pinite that had the highest caesium abundances, the chloride abundance
752 could not be determined.

753

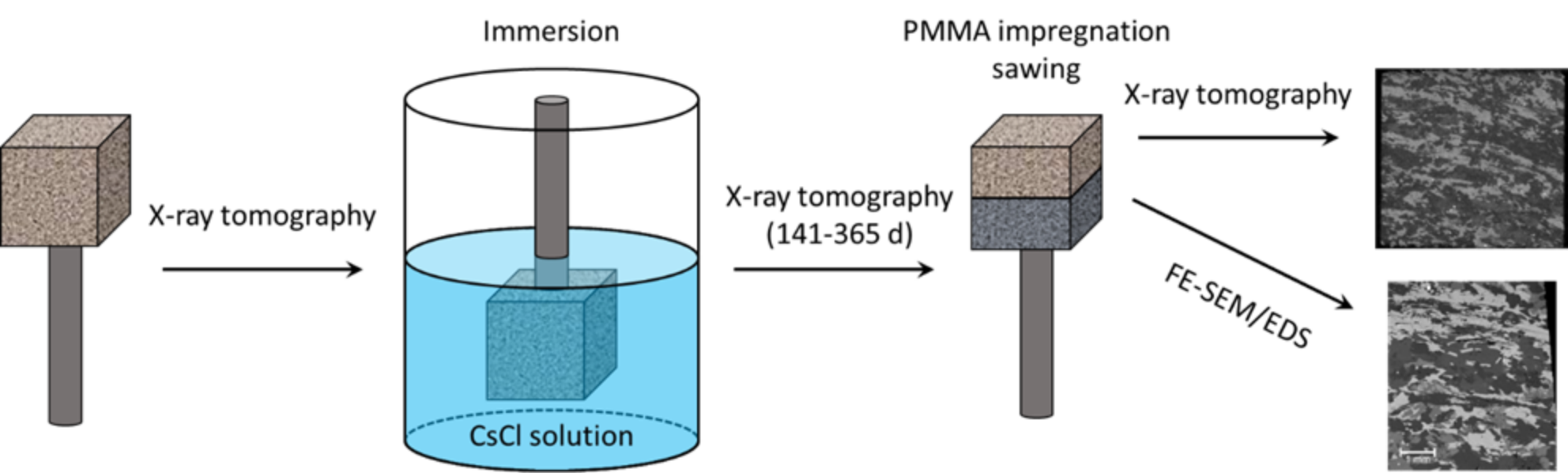
Immersion
PMMA impregnation
sawing
X-ray tomography
X-ray tomography
X-ray tomography
(141-365 d)
X-ray tomography
FE-SEM/EDS
CsCl solution

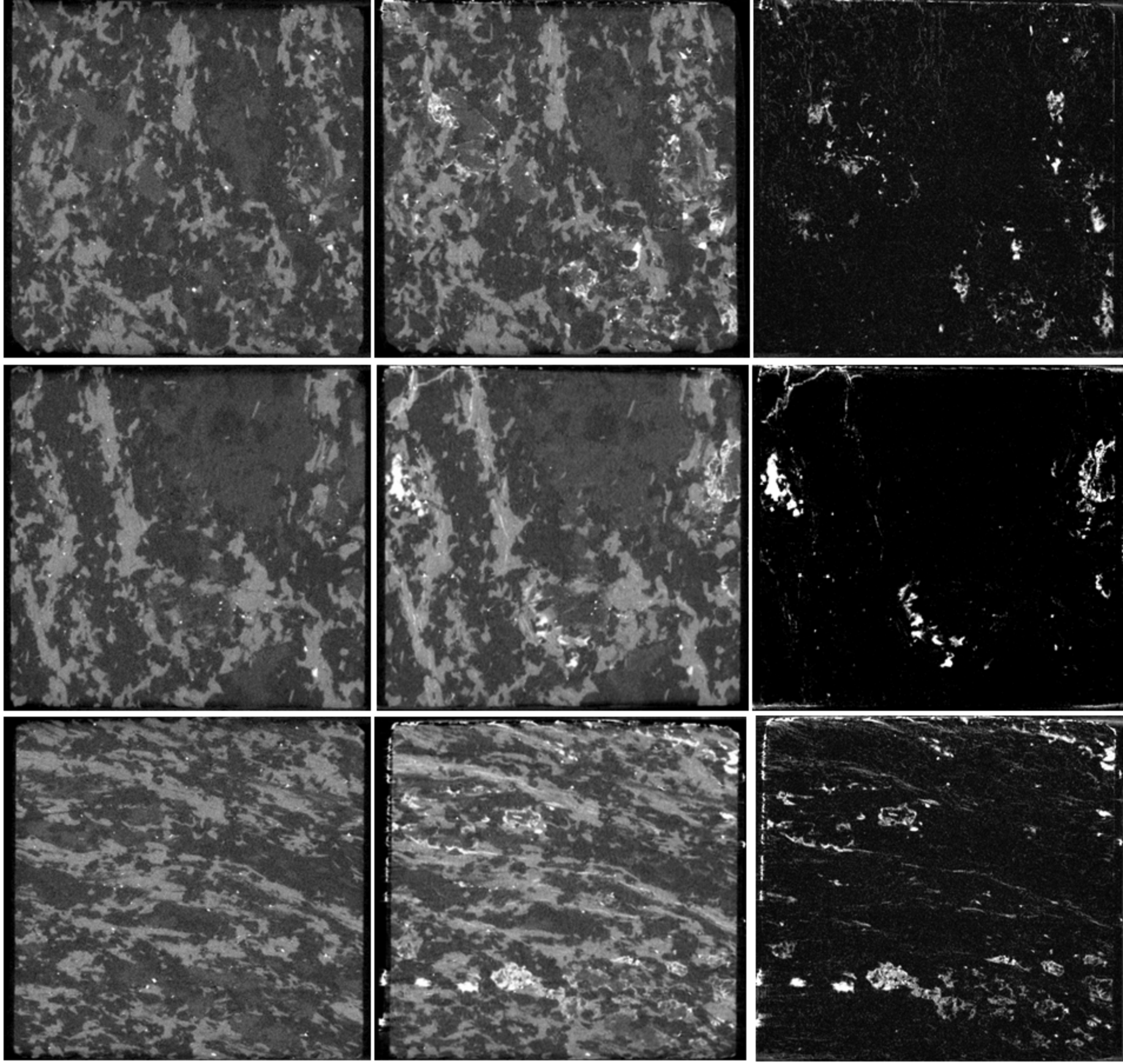
141 d
249 d
365 d
Before
After
Difference

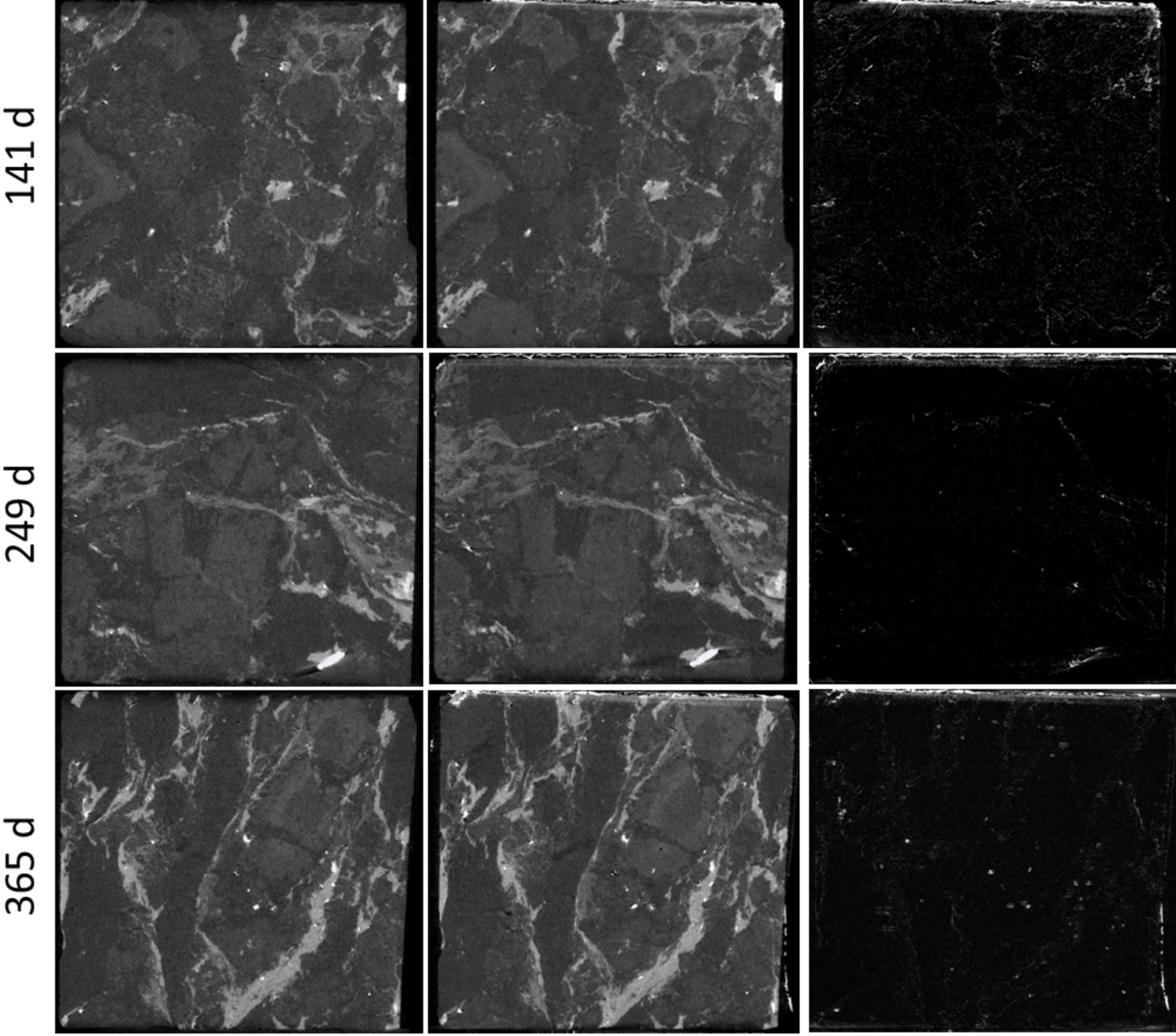
141 d
249 d
365 d
Before
After
Difference

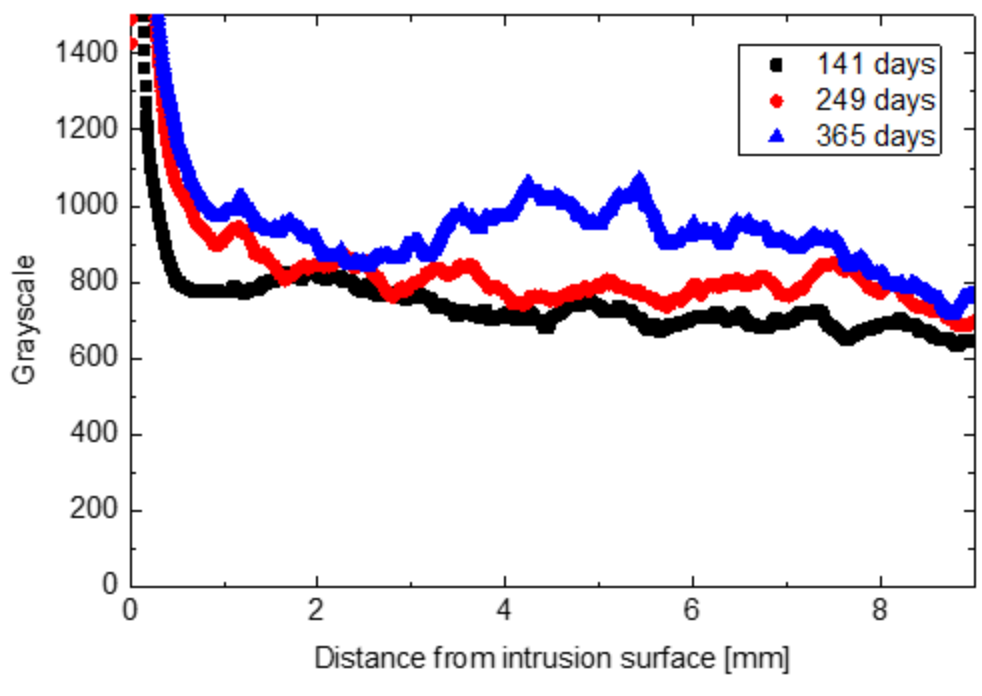
141 days
249 days
365 days
Grayscale
Distance from intrusion surface [mm]
0
200
400
600
800
1000
1200
1400
0
2
4
6
8

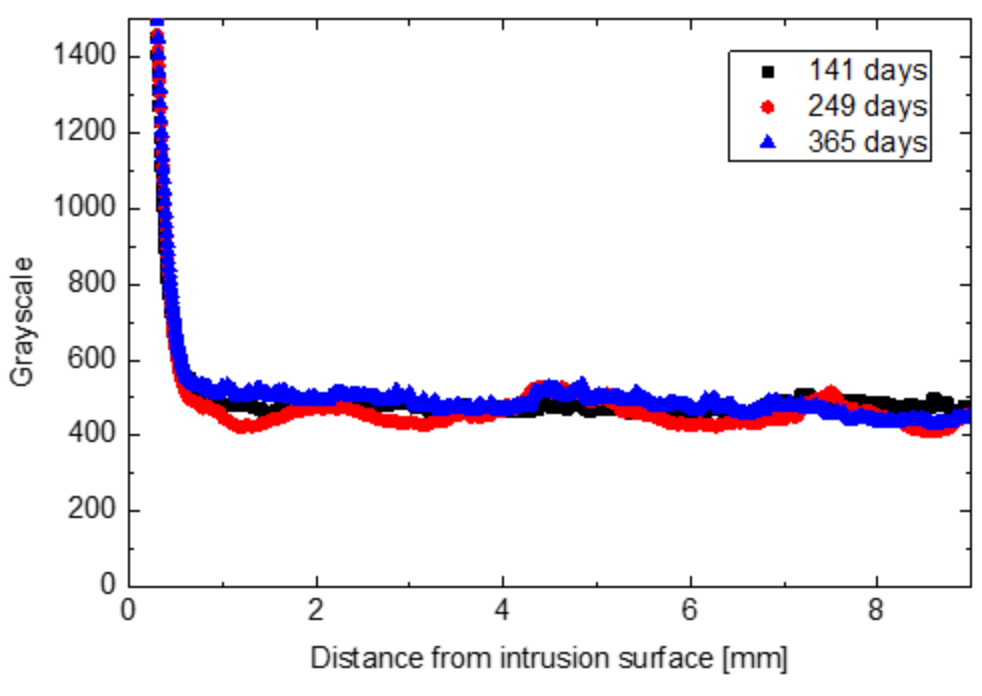
141 days
249 days
365 days
Grayscale
Distance from intrusion surface [mm]
0
200
400
600
800
1000
1200
1400
0
2
4
6
8

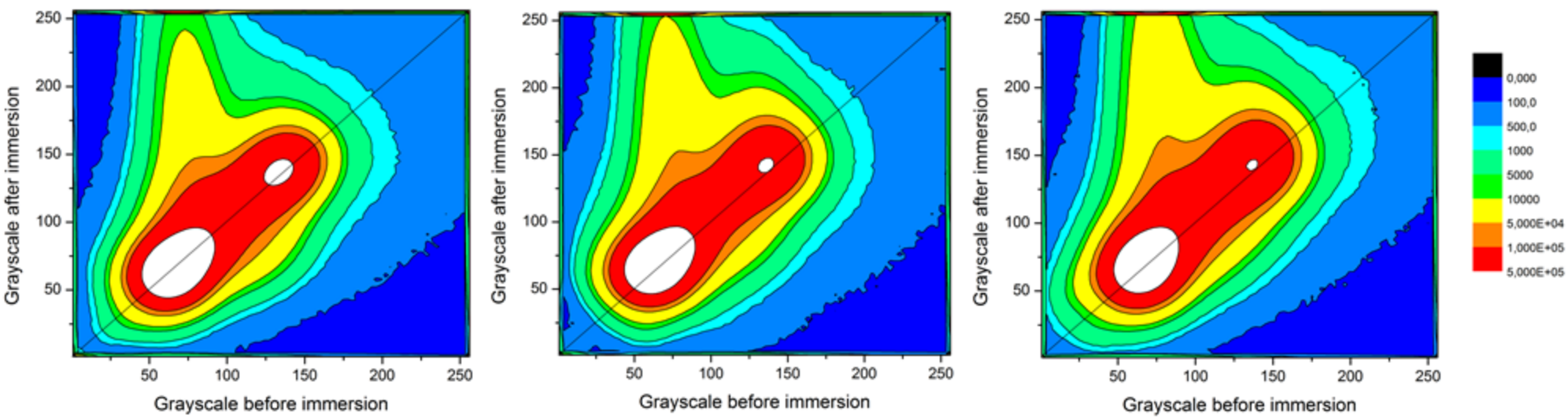
Grayscale after immersion
Grayscale before immersion
250
200
150
100
50
50
100
150
200
250
0,000
100,0
500,0
1000
5000
10000
5,000E+04
1,000E+05
5,000E+05

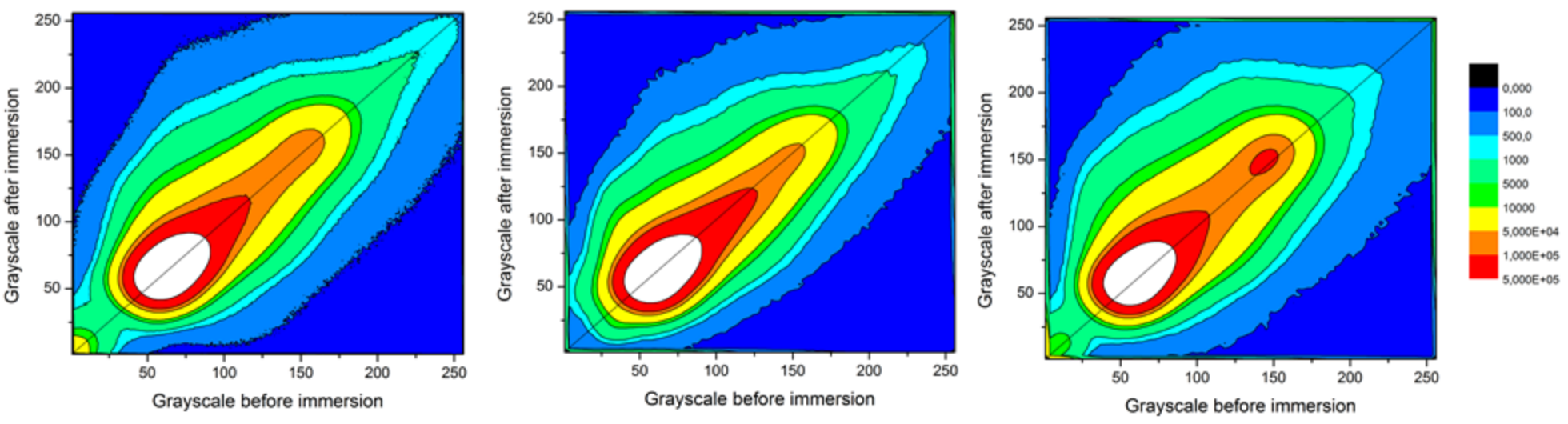
Grayscale after immersion
Grayscale before immersion
250
200
150
100
50
50
100
150
200
250
0,000
100,0
500,0
1000
5000
10000
5,000E+04
1,000E+05
5,000E+05

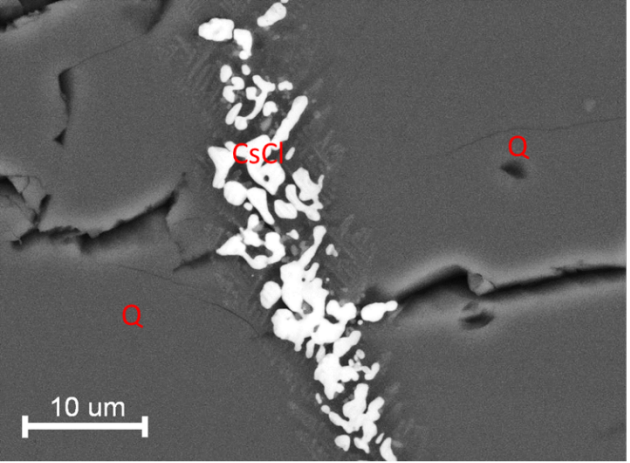
CsCl
Q
Q
10 um

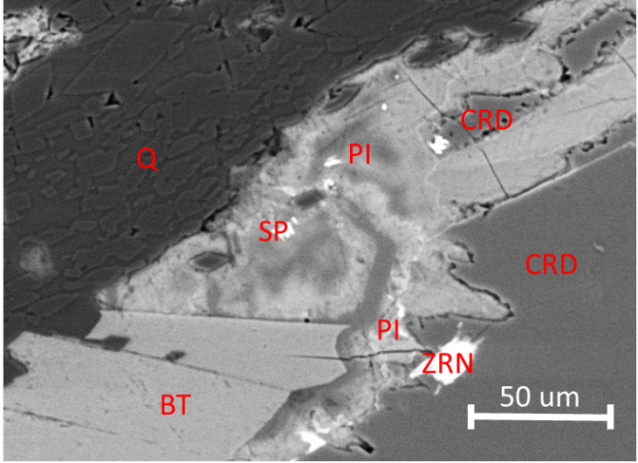
Q
PI
CRD
SP
CRD
PI
ZRN
BT
50 um

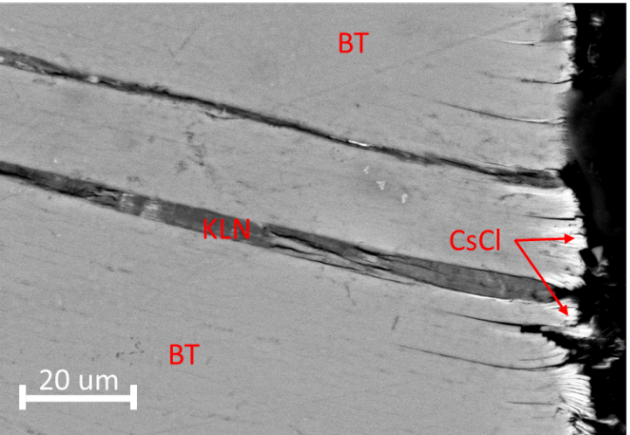
BT
KLN
CsCl
BT
20 um

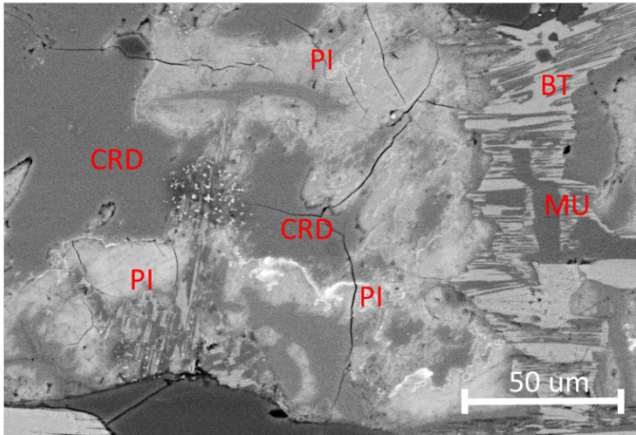
PI
BT
CRD
MU
CRD
PI
PI
50 um

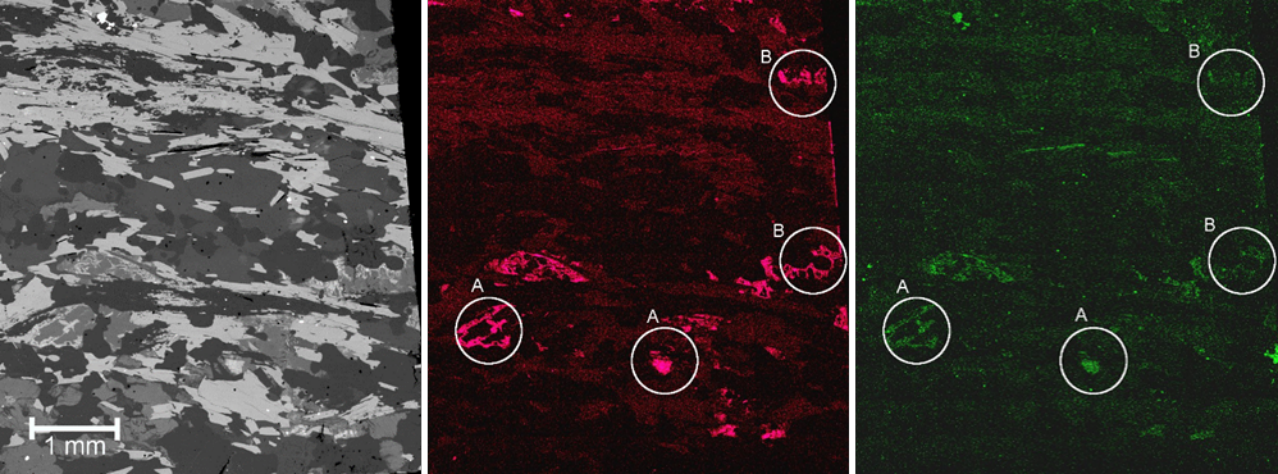
1 mm
A
A
B
B
A
A
B
B

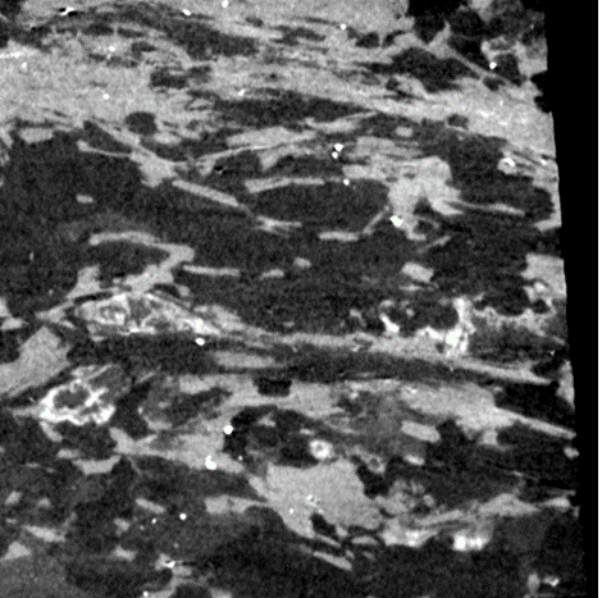

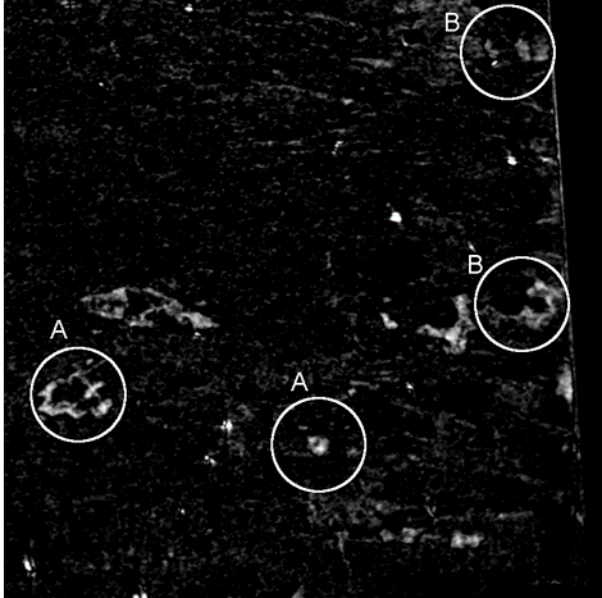
B
B
A
A

Table 1. Caesium and chloride abundances in atomic% and their ratios sorted by the minerals where they were found in notable amounts. The values given are averages with the ranges given in brackets. In few areas of pinite that had the highest caesium abundances, the chloride abundance could not be determined.

Mineral	**Cs atomic %**	**Cl atomic %**	**Cs-Cl-ratio**
Pinite	1.9 (1.3-2.8)	0.6 (0.4-1.1)	3.5 (2.0-6.3)
	5.4 (2.1-8.0)	No Cl detected	-
Kaolinite	0.9 (0.4-1.2)	0.9 (0.4-1.2)	1.0 (0.9-1.1)
Sphalerite	1.2	No Cl detected	-